Estimation of Size and Shape Information of Non-Spherical Particles Using FBRM

Okpeafoh S. Agimelen[a], Jan Sefcik[a], Massimiliano Vasile[b], Alison Nordon[c], Ian Haley[d], Anthony J. Mulholland[e]

[a]*Department of Chemical and Process Engineering, University of Strathclyde, James Weir Building, 75 Montrose Street, Glasgow, G1 1XJ, United Kingdom.*
[b]*Department of Mechanical and Aerospace Engineering, University of Strathclyde, James Weir Building, 75 Montrose Street, Glasgow, G1 1XJ, United Kingdom.*
[c]*Department of Pure and Applied Chemistry and Centre for Process Analytics and Control Technology, University of Strathclyde, 295 Cathedral Street, Glasgow, G1 1XL, United Kingdom*
[d]*Mettler-Toledo Ltd., 64 Boston Road, Beaumont Leys Leicester, LE4 1AW, United Kingdom*
[e]*Department of Mathematics and Statistics, University of Strathclyde, Livingstone Tower, 26 Richmond Street, Glasgow G1 1XH, United Kingdom*

Abstract

The recovery of crystal size and shape information insitu during drug manufacture is a major challenge. This information is very important because the suitability of these particles for further processing depends on their size and shape among other factors. The online focused beam reflectance measurement sensor measures the chord length distribution (CLD) of the particles. Recovery of size and shape information from the CLD requires knowledge of the range of particle sizes in the population.

This paper presents an algorithm which allows size and shape information to be recovered from the CLD data without the additional information on the range of particle sizes in the population. The particle size and shape information recovered by the algorithm shows good agreement with measurements by laser diffraction and image analysis.

Email addresses: okpeafoh.agimelen@strath.ac.uk (Okpeafoh S. Agimelen), jan.sefcik@strath.ac.uk (Jan Sefcik), massimiliano.vasile@strath.ac.uk (Massimiliano Vasile), alison.nordon@strath.ac.uk (Alison Nordon), Ian.haley@mt.com (Ian Haley), anthony.mulholland@strath.ac.uk (Anthony J. Mulholland)

Keywords: Chord Length Distribution, Particle Size Distribution, Particle Shape, Focused Beam Reflectance Measurement.

1. Introduction

The process of drug manufacture includes the formation of an active pharmaceutical ingredient (API) in solution with various impurities. This API is then separated from the impurities by crystallisation which leads to the formation of solid particles (crystals) of various shapes and sizes. Further processing of the API requires an accurate knowledge of its size and shape. Different techniques including sieving, electrical zone sensing, laser diffraction, microscopy, focused beam reflectance measurement (FBRM) and so on [1, 2] are employed to determine size and shape information. The FBRM technique is particularly attractive because (the probe is designed in such a way that) it can be used in situ during the production process. Hence there has been a considerable effort [3–15] devoted towards obtaining useful information about particle population from this technique. This has led to the development of both 2 D and 3 D models [3–9, 11–15] for obtaining size and shape information from FBRM data. The simple 2 D models have some short comings [12] because of the simplifying assumptions made in their formulation. However, the more advanced 3 D models may not give complete information if they do not take the optical properties of the relevant materials into account [15].

The inverse problem of retrieving size and shape information from FBRM data is non trivial [2]. The degree of accuracy of the solution depends on the model used and the method for calculating the solution with a particular model. The early models [16–18] of FBRM were based on populations of spherical particles [1]. While these models can give reasonable estimates (if appropriate methods of solution are used) of particle sizes, they are not suitable for particles whose shape deviate significantly from spherical.

However, some progress has been made towards modelling particle populations whose shape deviate (by various extents) from spherical [4, 8–11] with promising results. One factor which influences the accuracy of solutions obtained with these models is the size range of particles used in the calcula-

[1]The problem is significantly simplified for spherical particles due to the symmetry properties of the sphere.

tions. In the work by Ruf et al [4] information about particle size range was obtained by a laser diffraction technique and microscopy. While Worlitschek et al. [8] obtained particle size range information by sieving similar to the case of Li et al. [10]. Finally, Kail et al. [14] obtained information about particle size range in their population of particles from the manufacturer. However, information about particle size range may not be readily available or it may not be convenient to obtain this information (for example in a production process).

When moving from modelling of single particles to a population of particles, it is necessary to account for size effects. It has been demonstrated [11, 16, 17, 19] that larger particles have a higher probability to be detected by the FBRM probe. While this effect has been taken into account in some cases [4, 8] it has been neglected in some other cases [9, 10]. This negligence may not introduce a large error in a population of particles of a narrow size distribution. However, the error could be significant if the size range of particles in the population is large.

Even though there has been some progress in retrieving size and shape information (from FBRM data) in population of particles with different degrees of variation from spherical [4, 8–10], there has been no attempt to obtain size and shape information in populations of needle shaped particles using simple models. This is despite the fact that there are simple models [9, 11] in the literature which can be used to obtain useful size and shape information in needle shaped particles.

A problem which arises from the mathematically ill posed nature of the inverse problem is the situation whereby the solution contains negative particle sizes. Despite the fact that different methods have been proposed [8, 9] to avoid this possibility, there is still room for other methods that can be readily implemented with existing numerical packages.

In this paper, we present the first estimate of size and shape information of needle shaped particles using simple models. Furthermore, one of the models (Vaccaro-Sefcik-Morbidelli [11]) has never been implemented before. We validate the calculations with data obtained by dynamic image analysis and laser diffraction. We also introduce a technique for obtaining the size range of particles in a population directly from the FBRM data without relying on information from other sources. By formulating the inverse problem as a nonlinear least square optimisation problem we obtain solutions that are guaranteed to contain non negative particle sizes. The nonlinear least square problem is easily implemented in existing numerical packages. We

also incorporate the effect of length weighting (by particles of different sizes) in the FBRM data in our calculations to increase the degree of accuracy.

Here we use 2 D models which are most suitable for opaque particles. However, the technique can be extended to materials with different optical properties given a model which incorporates these properties.

2. Principle of the FBRM

The FBRM technology involves a laser beam which is focused onto a spot by a system of lenses. The laser spot is focused near a sapphire window where it is rotated along a circular path at a speed of about 2ms^{-1} [2, 7, 12, 13]. The assembly of lenses is enclosed in a tubular probe which is inserted into a slurry of dispersed particles. Particles passing near the probe window reflect light back into the probe which is then detected. It is assumed that the particles are much smaller than the diameter of the circular trajectory of the laser beam, and the particles move much more slowly than the speed of the laser spot [2]. Hence the length of arc (taken to be a straight line) made by the laser spot on a particle from which light is scattered is just a product of the speed of the laser spot and the duration of reflection [2], and the corresponding chord length is recorded. Since the beam does not always pass through the centre of the particle, a range of chord lengths is recorded as a given particle encounters the beam multiple times. The FBRM device accumulates chord lengths across different particles present in the slurry for a duration pre-set by the user, after which it reports a chord length histogram.

Figure 1: The samples of COA after undergoing different drying conditions in the vacuum agitated drier [20]. The samples in (a) to (e) are labelled Sample 1 to Sample 5 in Figs. 2 and 3. The white horizontal line on the bottom right of (a) indicates a length of 100μm. Reproduced by permission of The Royal Society of Chemistry (View Online).

3. Experimental Data

For the purpose of demonstrating and validating our technique, we shall apply the method (to be described in subsequent sections) to data obtained

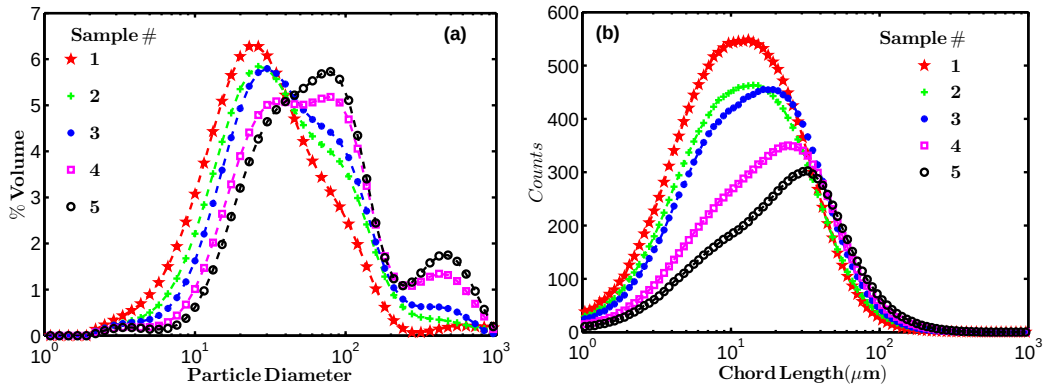

Figure 2: (a) Volume weighted particle size distribution obtained with the Malver Mastersizer and (b) chord length distribution from the FBRM probe for the samples in Fig. 1.

in a previous study [20]. Five samples (sample 1 to sample 5) of needle-shaped particles of cellobiose octaacetate (COA) that had been subjected to different drying conditions [21] were analysed by laser diffraction, FBRM and dynamic image analysis. The drying conditions used caused different degrees of particle attrition as shown in Fig. 1. Samples were dispersed in 0.1% Tween 80 (Sigma-Aldrich, UK) in water for all particle size measurements. Laser diffraction measurements were carried out using a Malvern Mastersizer 2000 (Malvern Instruments, UK). FBRM data were obtained using a Lasentec FBRM PI-12/206 probe. Dynamic image analysis was carried out using a QICPIC (Sympatec Ltd., UK) instrument with a LIXELL wet dispersion unit. Further experimental details for the particle size analysis techniques employed can be found in [20].

The particle size estimated by laser diffraction, which assumes that the particles are spherical, for samples 1 to 5 is shown in Fig. 2(a). The FBRM chord length distribution obtained for the five samples is shown in Fig. 2(b). The equivalent projected circle EQPC diameter (which is the diameter of a circle of equal area to the 2 D projection of a particle) obtained by dynamic image analysis is shown in Fig. 3(a). The maximum Feret diameter (Feret Max)[2] obtained using dynamic image analysis, which was shown to be the best indicator of needle length [20] is shown in Fig. 3(b). In addition, the Feret Min diameter (Feret Min) which is an indication of needle width is

[2]See [19] and [20]for further description of the concepts of Feret diameter and EQPC.

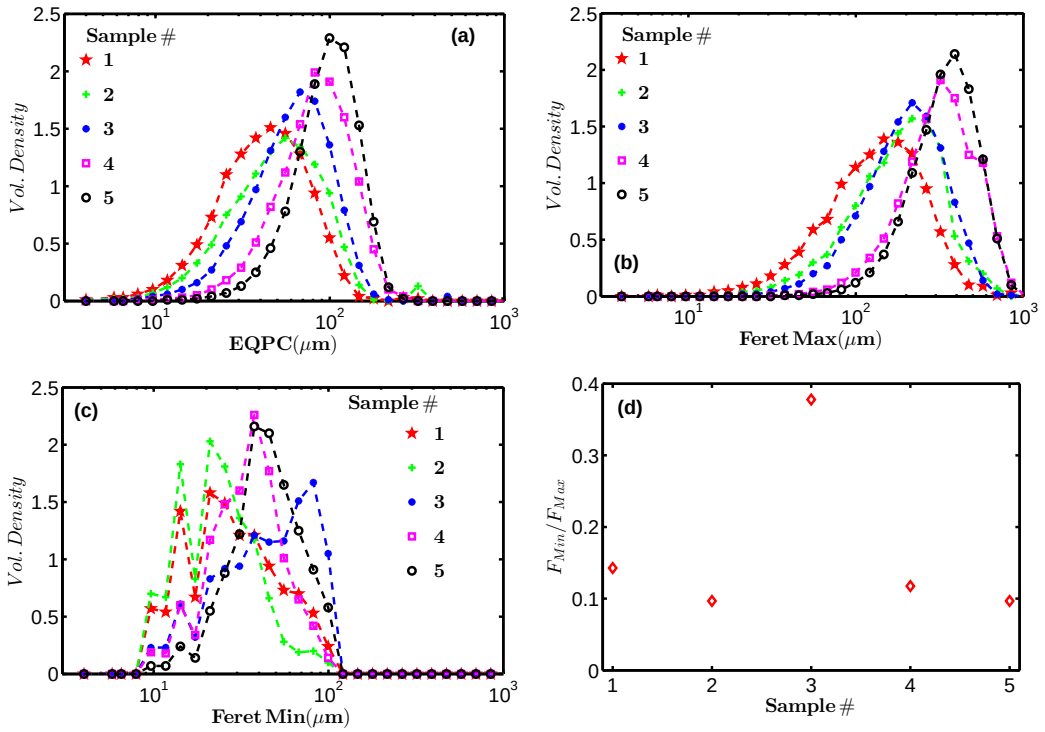

Figure 3: (a) Volume weighted EQPC diameter, maximum Feret diameter (b), and minimum Feret diameter (c) obtained by dynamic image analysis for the samples in Fig. 1. (d) A measure of the degree of elongation of the needles in Fig. 1.

shown in Fig. 3(c). The degree of elongation of the needles can be estimated by computing the ratio of the modes of the Feret Min distributions to the modes of the Feret Max distributions. The result (F_{min}/F_{max}) of this calculation is shown in Fig. 3(d). The data in Figs. 2 and 3 will be used to validate the algorithm described in section 5 [19].

4. Modelling

The key feature of the FBRM technology is that it reports a chord length distribution (CLD) rather than the actual particle size distribution (PSD). Although the CLD and PSD are related to each other, the CLD obtained from a given particle depends on both its size and shape. This size and shape information is encoded in a kernel function which relates the measured CLD to the unknown PSD. However, in a population of particles, the

probability of a particle to be detected depends on its characteristic size D [4, 8, 11, 16, 17, 19]. Hence the PSD is weighted by the characteristic sizes of the particles in the population. The characteristic size of each particle is a monotonic function of some length scale associated with the particle [8]. This function depends on the shape of the particle [11]. For example, the case of a population of spherical particles of different sizes will result in $D = 2a_s$, where a_s is the radius of a sphere. Thus the relationship between the CLD and PSD can be written as [16]

$$C(L) = \int_0^\infty A(D, L)DX(D)dD, \tag{1}$$

where C is the CLD, A is the kernel function, L is chord length and X is the PSD. Equation (1) can be discretised and written in matrix form as [9, 16]

$$\mathbf{C} = \mathbf{A}\tilde{\mathbf{X}}, \tag{2}$$

where $\mathbf{A}$ is a transformation matrix. The column vector $\mathbf{C}$ is the chord length histogram or CLD [3], while the column vector $\tilde{\mathbf{X}}$ is defined as

$$\tilde{X}_i = D_i X_i, \tag{3}$$

where $\mathbf{D}$ is the vector of characteristic sizes and $\mathbf{X}$ is the unknown PSD. Equation (2) can be rearranged so that each component of $\mathbf{D}$ multiplies a column of $\mathbf{A}$ to give

$$\mathbf{C} = \tilde{\mathbf{A}}\mathbf{X}, \tag{4}$$

where

$$\tilde{A}_j = [a_{j,1}D_1 \; a_{j,2}D_2 \; \ldots \; a_{j,i}D_i \; \ldots \; a_{j,N}D_N], \tag{5}$$

represents column j of $\tilde{\mathbf{A}}$.

The matrix $\mathbf{A}$ is of dimension $M \times N$, where M is the number of chord length bins in the histogram $\mathbf{C}$ and N is the number of particle size bins in the histogram $\mathbf{X}$ [9]. The columns of matrix $\mathbf{A}$ are constructed as [9]

$$A_j = [a_{j,1} \; a_{j,2} \; \ldots \; a_{j,i} \; \ldots \; a_{j,N}], \tag{6}$$

where

$$a_{j,i} = p_{\overline{D}_i}(L_j, L_{j+1}) \tag{7}$$

[3] For simplicity we refer to the matrices $\mathbf{C}$ and $\mathbf{X}$ as 'distributions'. Although strictly speaking they are not distribution functions since they have been discretised.

is the probability that the length of a measured chord from a particle of characteristic size $\overline{D}_i$ lies between L_j and L_{j+1}. The characteristic size of particles bounded by the bin boundaries D_i and D_{i+1} is given as $\overline{D}_i = \sqrt{D_i D_{i+1}}$. The probabilities $p_{\overline{D}_i}(L_j, L_{j+1})$ for different particle sizes and chord length bins are calculated from appropriate probability mass functions (PMF). The PMFs employed in this work are those given by the Vaccaro-Sefcik-Morbidelli (VSM) [11] model and the Li-Wilkinson (LW) model [9].

The forward problem of calculating the CLD from a known PSD using Eq. (4) is trivial as it is mere matrix multiplication. However, the inverse problem of calculating the PSD from a known CLD is non trivial. The solution vector $\mathbf{X}$ must meet the requirement of non negativity, hence different techniques have been used in the past [8, 9] to fulfil this requirement. There could also be errors in the solution vector $\mathbf{X}$ if the transformation matrix $\mathbf{A}$ is inaccurate. The accuracy of the matrix $\mathbf{A}$ depends on the particle size range and the model used in calculating the probabilities in Eq. (7). Here we shall describe a technique to select the most appropriate particle size range. Then suitable models are chosen based on information from microscope images. The method employed here also guarantees the non negativity requirement of the solution vector $\mathbf{X}$.

4.1. The VSM model

The microscope images in Fig. 1 suggest that the shape of the particles could be represented by thin cylinders. The 2 D projections of these thin cylinders will look like the shapes in Fig. 1. The cylindrical VSM model [11] gives a PDF X_p^c which defines the relative likelihood that a chord taken from a cylindrical particle has a length between L and $L + dL$. To this end, the model considers all possible 3 D orientations of each cylindrical particle and calculates chord lengths from each 2 D projection. Hence we calculate the characteristic size of a cylinder by equating the diameter of a sphere of equivalent volume. This then gives $D_c = a_c \sqrt[3]{3r_c^2/2}$. For a thin cylinder of height a_c and base radius b_c, the VSM model gives the probability X_p^c (for $b_c/a_c \ll 1$) as [11]

$$a^* X_p^c(L) = \begin{cases} \frac{1}{2} \frac{L}{\sqrt{r_c^2 a_c^2 - L^2}} \left(1 - \sqrt{1 - r_c^2}\right), & \forall L \in [0, r_c a_c[\\ \frac{1}{\pi} \frac{r_c^2}{\sqrt{1 - \left(\frac{L}{a_c}\right)^2}} + \frac{1}{2\pi} \frac{a_c}{L} \frac{\frac{L}{a_c}\sqrt{1 - \left(\frac{L}{a_c}\right)^2} + \cos^{-1}\left(\frac{L}{a_c}\right)}{\frac{L}{r_c a_c}\sqrt{\left(\frac{L}{r_c a_c}\right)^2 - 1}} & \forall L \in]r_c a_c, a_c[\\ 0 & \forall L \in [a_c, \infty[, \end{cases} \tag{8}$$

where $r_c = 2b_c/a_c$ is the aspect ratio of the thin cylinder and

$$a^* = \frac{a_c}{4} + \frac{1}{2} r_c a_c \left[1 - \sqrt{1 - r_c^2} + \frac{1}{2} r_c \left(1 - \frac{4}{\pi} \sin^{-1}(r_c) \right) \right] \tag{9}$$

is a normalisation factor. Then the probability that the length of a measured chord from a particle of size D_c falls in the bin bounded by L_j and L_{j+1} is calculated as

$$p_{c\overline{D}_i}(L_j, L_{j+1}) = \int_{L_j}^{L_{j+1}} X_p^c(L) dL. \tag{10}$$

The integration in Eq. (10) is performed numerically.

4.2. The LW model

In this case, we approximate the shape of the needles in Fig. 1 by thin ellipsoids. The 2 D projection of each of these ellipsoids will be an ellipse of semi major axis length a_e, semi minor axis length b_e and aspect ratio $r_e = b_e/a_e$. The length of a chord on this ellipse depends on the angle α between the chord and the x axis (where the projection plane is the $x - y$ plane) [9]. Hence the PMF for such an ellipse is angular dependent. The PMF for different values of α are given by the LW model as [9]:
for $\alpha = 0$ or π

$$p_{e\overline{D}_i}(L_{j,\alpha}, L_{j+1,\alpha}) = \begin{cases} \sqrt{1 - \left(\frac{L_j}{2a_{ei}}\right)^2} - \sqrt{1 - \left(\frac{L_{j+1}}{2a_{ei}}\right)^2}, & \text{for } L_j < L_{j+1} \leq 2a_{ei} \\ \sqrt{1 - \left(\frac{L_j}{2a_{ei}}\right)^2}, & \text{for } L_j \leq 2a_{ei} < L_{j+1} \\ 0, & \text{for } 2a_{ei} < L_j < L_{j+1}, \end{cases} \tag{11}$$

for $\alpha = \pi/2$ or $3\pi/2$

$$p_{e\overline{D}_i}(L_{j,\alpha}, L_{j+1,\alpha}) = \begin{cases} \sqrt{1 - \left(\frac{L_j}{2r_e a_{ei}}\right)^2} - \sqrt{1 - \left(\frac{L_{j+1}}{2r_e a_{ei}}\right)^2}, & \text{for } L_j < L_{j+1} \leq 2r_e a_{ei} \\ \sqrt{1 - \left(\frac{L_j}{2r_e a_{ei}}\right)^2}, & \text{for } L_j \leq 2r_e a_{ei} < L_{j+1} \\ 0, & \text{for } 2r_e a_{ei} < L_j < L_{j+1}, \end{cases} \tag{12}$$

for other values of α

$$p_{e\overline{D}_i}(L_{j,\alpha}, L_{j+1,\alpha}) = \begin{cases} \sqrt{1 - \frac{r_e^2+s^2}{1+s^2}\left(\frac{L_j}{2r_e a_{ei}}\right)^2} \\ -\sqrt{1 - \frac{r_e^2+s^2}{1+s^2}\left(\frac{L_{j+1}}{2r_e a_{ei}}\right)^2}, & \text{for } L_j < L_{j+1} \leq 2r_e a_{ei}\sqrt{\frac{1+s^2}{r_e^2+s^2}} \\ \sqrt{1 - \frac{r_e^2+s^2}{1+s^2}\left(\frac{L_j}{2r_e a_{ei}}\right)^2}, & \text{for } L_j \leq 2r_e a_{ei}\sqrt{\frac{1+s^2}{r_e^2+s^2}} < L_{j+1} \\ 0, & \text{for } 2r_e a_{ei}\sqrt{\frac{1+s^2}{r_e^2+s^2}} < L_j < L_{j+1}, \end{cases} \tag{13}$$

where $s = \tan(\alpha)$. The angle independent PMF is then given as

$$p_{e\overline{D}_i}(L_j, L_{j+1}) = \frac{1}{2\pi}\int_0^{2\pi} p_{e\overline{D}_i}(L_{j,\alpha}, L_{j+1,\alpha})d\alpha. \tag{14}$$

Equation (14) allows the construction of the transformation matrix $\mathbf{A}$ in Eq. (2) which can be converted to the matrix $\tilde{\mathbf{A}}$ as described in Eq. (5). The matrix $\tilde{\mathbf{A}}$ is then used to solve the inverse problem.

The LW model constructs the PMF of an ellipsoidal particle by considering only one 2 D projection of the ellipsoid where the major axis is parallel to the projection plane. Hence the monotonic function which gives the characteristic size D_e of the resulting ellipse is obtained from the area of a circle of equivalent area. Hence, using $r_e = b_e/a_e$, the characteristic size is given as $D_e = 2a_e\sqrt{r_e}$.

5. Inversion Algorithm

The inversion algorithm starts by choosing an aspect ratio r and then constructing the matrix $\mathbf{A}$ in Eq. (2). The calculation of the matrix $\mathbf{A}$ requires information on the size range of particles in the population. That is, the characteristic sizes of the first particle size bin ($\overline{D}_1$) and the last particle size bin ($\overline{D}_N$). With this information the particle sizes can be split into N bins. The sizes of particles in the particle size bins are then used to calculate the columns of matrix $\mathbf{A}$ as described in Eq. (6).

To gain more accuracy in the particle size range (and without relying on information from other sources) we have formulated a procedure which uses the measured chord lengths directly. The process is carried out in such a way that different matrices $\mathbf{A}$ (corresponding to different size ranges) are

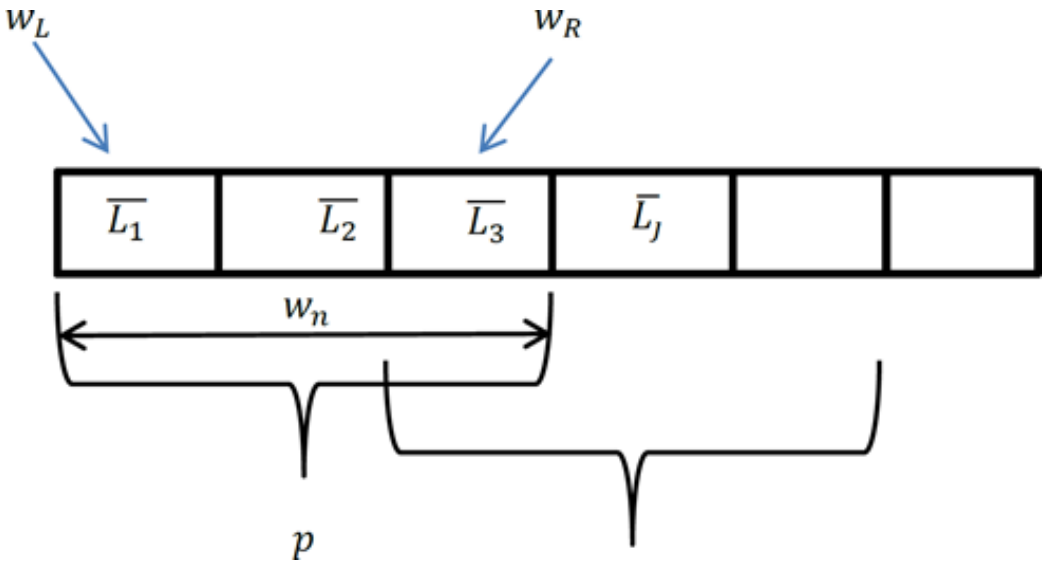

Figure 4: Pictorial representation of a measured chord length vector showing a window w_n at a position set by p. The window is moved in such a way that some of the elements of the chord length vector contained in the set defined by the initial position of the window overlap with the elements in the set defined by the succeeding window position.

constructed. The most accurate matrix (corresponding to the most accurate size range) is then selected. The procedure is outlined below.

The chord lengths

$$L_j,\ j = 1, 2, 3, \ldots, M \tag{15}$$

measured by the FBRM device are put in a vector as shown in Fig. 4. The characteristic chord length $\overline{L}_j$ of bin j is the geometric mean of the chord lengths of its boundaries

$$\overline{L}_j = \sqrt{L_i L_{j+1}}. \tag{16}$$

We then pick a window w_n of chord lengths which is the set $w_n \in [w_L, w_R]$ as indicated in Fig. 4. The size $S_w \geq 2$ of the window w_n is the number of elements (that is $\overline{L}$) in the set defined by w_n. For example, $S_w = 3$ in Fig. 4. Since the chord lengths follow a geometric progression, the boundary elements of each window are obtained as

$$w_L = \overline{L}_1 \beta^{(p-1)q} \tag{17a}$$

$$w_R = w_L \beta^{[S_w - 1]}, \tag{17b}$$

where $\beta = \overline{L}_{j+1}/\overline{L}_j$, the integer $q < S_w$ sets the step size of the window as it slides along the chord length vector. Smaller values of q give more accurate calculations but longer computational times. The windows are overlapping, and the step size is the number of bins between the beginning of a window and the beginning of the next window ($q = 2$ in Fig. 4). The integer

$$p = 1, 2, 3, \ldots, \left\lfloor \frac{M}{q} \right\rfloor, \tag{18}$$

where the floor function $\lfloor \cdot \rfloor$ returns the value of the largest integer that is less than or equal to M/q sets the window position as indicated in Fig. 4. As the integer p is increased, the window slides along the chord length vector. Windows of different sizes are used in this manner and each time the transformation matrix $\mathbf{A}$ is constructed using an appropriate PMF.

The chord lengths reported by the FBRM sensor run from 1μm to 1000μm. However, the particle size range $[\overline{D}_1, \overline{D}_N]$ set by a window will not necessarily cover the entire size range of 1μm to 1000μm. To account for the other sizes that may not be covered by a window, the length weighted transformation matrix $\tilde{\mathbf{A}}$ is augmented with columns of 1s as appropriate. Then the particle sizes are extended to the left of $\overline{D}_1$ down to 1μm and to the right of $\overline{D}_N$ up to 1000μm as appropriate. This ensures that the recovered PSD covers the entire particle sizes from 1μm to 1000μm. The process of augmenting the transformation matrix with columns of 1s corresponds to the addition of slack variables in an optimisation problem [19, 22].

To guarantee non negative PSD the vector $\mathbf{X}$ is written as [23]

$$X_i = e^{\gamma_i}, \;\; i = 1, 2, 3, \ldots, N, \tag{19}$$

where γ_i are arbitrary fitting parameters. Then Eq. (4) is rewritten as

$$\mathbf{C} = \tilde{\mathbf{A}}\mathbf{X} + \boldsymbol{\epsilon}, \tag{20}$$

where $\boldsymbol{\epsilon}$ is an additive error between the model prediction and the actual measurement. The vector $\mathbf{X}(r)$ at the chosen aspect ratio r is then obtained by searching for γ_i which minimises the objective function f_1 given as[4]

$$f_1 = \sum_{j=1}^{M} \left[C_j^* - \tilde{A}_{ji} X_i \right]^2, \tag{21}$$

[4]In all the calculations here a value of $N = 70$ was used for both VSM amd LW models [19].

where C_j^* is the measured CLD. This is a nonlinear least squares problem which was solved with the Levenberg-Marquardt (LM) algorithm. The Matlab implementation of this algorithm (used in this work) requires the nonlinear function to be defined. Then starting with an initial value for the vector γ_i the LM algorithm performs a successive iteration until an optimum γ_i is reached. The iterations are terminated when a specified tolerance in the difference between successive function evaluations is reached. In this case we used a tolerance of 10^{-6} since the results did not change for values of tolerance below 10^{-4} An initial value of $\boldsymbol{\gamma} = \mathbf{0}$ was used in the LM algorithm.

The solution vector $\mathbf{X}$ obtained this way (using Eq. (19)) is dependent on the chosen aspect ratio r (hence $\mathbf{X} = \mathbf{X}(r)$) and window position. Thus, starting with a window of a chosen size[5] and at position set at $p = 1$, a solution vector $\mathbf{X}(r)$ is obtained for the chosen aspect ratio. Then the forward problem is solved to obtain a CLD $\mathbf{C}(r)$ at that aspect ratio and window position $p = 1$. The window position is advanced one step forward and the calculation repeated until the end of the chord length vector is reached. The window position at which the L_2 norm

$$\|\mathbf{C}^* - \mathbf{C}(r)\| \tag{22}$$

is minimized is the optimum window position for that window size. This optimum window then sets the particle size range to construct the optimum transformation matrix $\mathbf{A}$ at that window size. The case of $S_w = 20$ applied to the chord length vector from Sample 1 for $N = 70$ (using the LW model) is shown in Fig. 5. The procedure is repeated using windows of different sizes and eventually obtaining the optimum window size and position which set the particle size range for the chosen aspect ratio. The whole process is repeated at different aspect ratios, and for each aspect ratio the particle size range is obtained from the optimum window size and position. The key steps of the algorithm are summarised below for clarity.

1. Choose a value of r.
2. Choose a window size S_w.
3. Start at $p = 1$.

[5]The values $q = 2$, initial window size $S_w = 6$ were used for both the VSM and LW models [19].

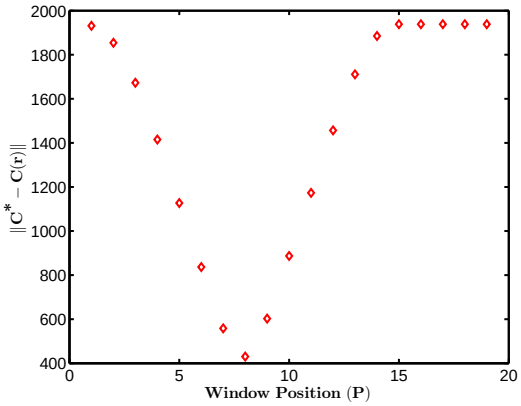

Figure 5: An example of the minimisation of the L_2 norm in Eq. (22) when a window of a given size approaches and passes its optimum position along a measured chord length vector.

4. Obtain the particle size range set by the window at the position set by p.

5. Construct matrix $\mathbf{A}$ corresponding to the particle size range in step 4.

6. Apply length weighting to matrix $\mathbf{A}$ using Eq. (5).

7. Augment matrix $\tilde{\mathbf{A}}$ with columns of 1s and extend particle size range as necessary.

8. Call LM algorithm to calculate $\boldsymbol{\gamma}$ starting with $\boldsymbol{\gamma} = \mathbf{0}$, then calculate $\mathbf{X}(r)$ from Eq. (19).

9. Calculate $\mathbf{C}(r)$ from Eq. (4).

10. Update p and repeat steps 4 to 9 for the same value of r until the end of the measured chord length vector is reached.

11. Calculate the L_2 norm in Eq. (22) for the given values of S_w and r.

12. Choose the best window position (the window position with the minimum L_2 norm as in Fig. 5) for the given values of S_w and r.

13. Update the window size and repeat steps 3 to 12.

14. For a given r obtain the window position and size at which the L_2 norm in Eq. (22) attains its minimum. Record the particle size range corresponding to this window position and size.

15. Update r and repeat steps 2 to 14.

Having obtained the optimum particle size ranges at different aspect ratios for a particular sample, then the optimum aspect ratio for that sample can be chosen using a suitable procedure. The simplest procedure would have been to pick the aspect ration at which the L_2 norm reaches its global minimum. However, the simulations show [19] that when the number of particle size bins is large enough the L_2 norm in Eq. (22) does not show a clear global minimum. Instead it decreases with increasing aspect ratio [19] and then levels off after some critical aspect ratio. Hence unique shape information cannot be obtained using the objective function in Eq. (21).

This problem of non uniqueness can be removed if the shape of the recovered PSD (X_i in Eq. (21)) is taken into account. As the aspect ratio deviates further from some reasonable value for a particular sample, the recovered PSD shows increasing degree of unphysical spikes [19]. This then motivates the formulation of a new objective function which mitigates these unphysical spikes by putting a restriction in the norm of the PSD. The new objective function f_2 is given as

$$f_2 = \sum_{j=1}^{M} \left[C_j^* - \tilde{A}_{ji} X_i \right]^2 + \lambda \sum_{i=1}^{N} X_i^2, \tag{23}$$

the parameter λ sets the level of penalty imposed on the norm of the PSD. The value of lambda is chosen by comparing the relative magnitude of the sum of squares in Eq. (23) [19]. The optimum particle size ranges at different aspect ratios obtained using the inversion algorithm above are used to construct the transformation matrix $\tilde{\mathbf{A}}$ (in Eq. (23)) at the corresponding aspect ratios. The optimum aspect ratio is chosen as the value of r at which the objective function f_2 reaches its global minimum for a carefully chosen value of λ [19]. The corresponding PSD at which f_2 reaches its global minimum is then chosen as the optimum PSD.

For a meaningful comparison of calculated PSD with experimentally measured PSD it is necessary that the calculated PSD be cast as a volume based distribution. This is because the measuring instruments report PSD in terms

of a volume based distribution for example Figs. 3(a), 3(b) and 3(c). The traditional approach of calculating the volume based PSD $\mathbf{X}^v$ as [24]

$$X_i^v = \frac{X_i^o \overline{D}_i^3}{\sum_i^N X_i^o \overline{D}_i^3}, \tag{24}$$

(where $\mathbf{X}^o$ is the optimum number based PSD which minimises the objective function f_2 in Eq. (23)) could lead to an artificial peak at large particle sizes if there are small fluctuations in the right tail of the number based PSD [19]. This situation requires that a suitable regularisation be applied to the recovered volume based PSD. However, a direct regularisation cannot be applied to the volume based PSD as it is calculated in Eq. (24). A new method for calculating the volume based PSD which allows direct application of a regularisation procedure is given below. Calculate the CLD C_j^o given by

$$C_j^o = \tilde{A}_{ji}^o \hat{X}_i^o, \tag{25}$$

where $\tilde{A}_{ji}^o$ is the optimum transformation matrix obtained by the inversion algorithm and

$$\hat{X}_i^o = \frac{X_i^o}{\sum_i^N X_i^o}. \tag{26}$$

The volume based PSD X_i^v can be written as

$$X_i^v = \frac{\hat{X}_i^o \overline{D}_i^3}{\sum_i^N \hat{X}_i^o \overline{D}_i^3}. \tag{27}$$

Substitution into Eq. (25) gives

$$C_j^o = \overline{A}_{ji}^o \overline{X}_i^v, \tag{28}$$

where

$$\overline{A}_{ji}^o = \frac{\tilde{A}_{ji}^o}{\overline{D}_i^3} \tag{29a}$$

$$\overline{X}_i^v = \left[\sum_i^N X_i^o \overline{D}_i^3 \right] X_i^v. \tag{29b}$$

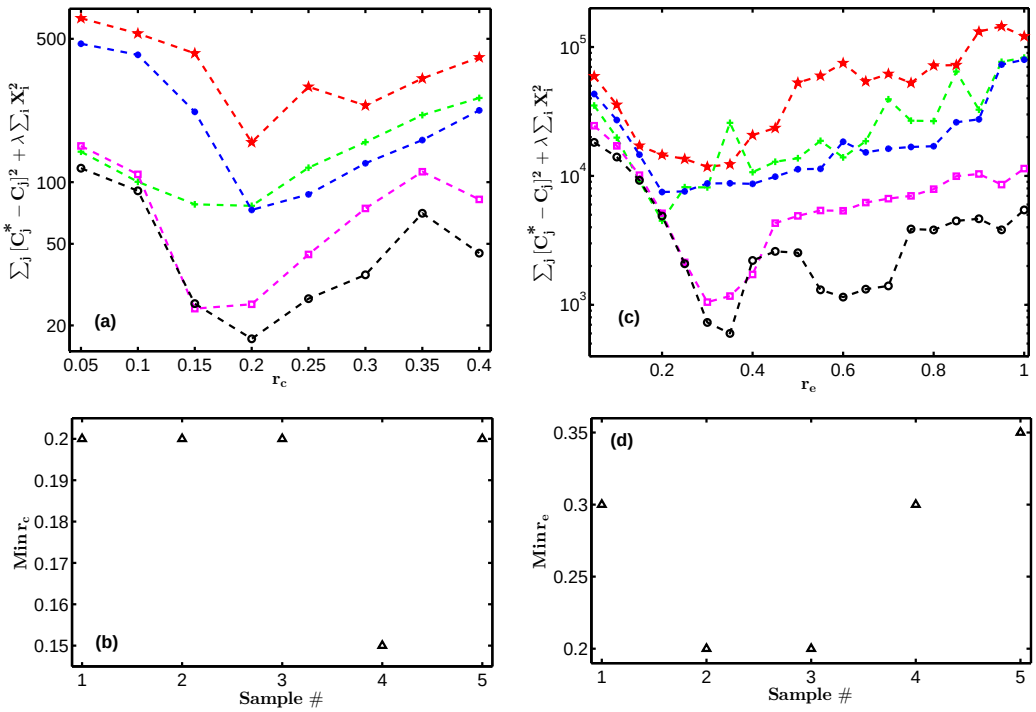

Figure 6: (a) Variation of the minimum values of the objective function in Eq. (23) with different aspect ratios (the minimum values of the objective function for all window sizes and positions for each sample indicated with symbols as: Sample 1 - red pentagrams, Sample 2 - green crosses, Sample 3 - blue asterisks, Sample 4 - magenta squares, Sample 5 - black circles) obtained with the VSM model at the specified aspect ratios. (b) The aspect ratios ($Min\ r_c$) at which the objective function reaches a global minimum for each Sample obtained with the VSM model. (c) Similar to (a) obtained with the LW model. (d) Similar to (b) with the LW model.

Since the quantities C_j^o and A_{ji}^o in Eq. (28) are known, then the unknown quantity $\overline{X}_i^v$ can be calculated by minimising the objective function f_3 given as

$$f_3 = \sum_{j=1}^{M} \left[C_j^o - \overline{A}_{ji}^o \overline{X}_i^v \right]^2 + \lambda \sum_{i=1}^{N} \left[\overline{X}_i^v \right]^2. \tag{30}$$

This allows $\overline{X}_i^v$ (obtained to some weighting factor due to Eq. (29)(b)) to be calculated as

$$\overline{X}_i^v = e^{\gamma_i^v},\ i = 1, 2, \ldots, N, \tag{31}$$

where γ_i^v is an arbitrary parameter which is used to minimise the objective

function f_3 for a carefully chosen λ [19]. The weighted volume based PSD is then normalised and made grid independent as

$$\tilde{X}_i^v = \frac{\overline{X}_i^v}{(D_{i+1} - D_i)\sum_i^N \overline{X}_i^v}. \tag{32}$$

6. Results/Discussions

Once the optimum particle size ranges at the different aspect ratios have been obtained using the inversion algorithm, then the optimum aspect ratio for each sample can be chosen by selecting the aspect ratio at which the objective function f_2 (in Eq. (23)) reaches its global minimum. The objective function f_2 at different aspect ratios $r_c \in [0, 0.4]$ for the five samples in Fig. 1 is shown in Fig. 6(a) for the case of the VSM model[6]. The function f_2 reaches its global minimum at $r_c \approx 0.2$ as in Fig. 6(b). The calculations with the VSM model is restricted to the range $r_c \in [0, 0.4]$ because the thin cylindrical VSM model is only valid for $r_c \ll 1$ [11].

Figure 6(c) shows a similar result to Fig. 6(a) for the same samples in Fig. 1. This is the case of the LW model. The function f_2 reaches its global minimum for $r_e \approx 0.3$ as in Fig. 6(d). In this case, the aspect ratios r_e cover a broader range $r_e \in [0, 1]$ since the LW model is valid for $r_e \in [0, 1]$. The aspect ratios predicted by the VSM and LW models in Figs. 6(b) and 6(d) are comparable to the aspect ratios estimated from image data in Fig. 3(d). However, the aspect ratios predicted in Figs. 6(b) and 6(d) are slightly higher than the estimated aspect ratios in Fig. 3(d) with the exception of sample 3 in Fig. 3(d) which may be an outlier.

The aspect ratios predicted by the VSM model in Fig. 6(b) are closer to the estimated aspect ratios in Fig. 3(d) when compared with the aspect ratios predicted by the LW model in Fig. 6(d). This could be because the VSM model gives better fit to the experimental data with the objective function f_1 in Eq. (21) [19] which is equivalent to $\lambda = 0$ in Eq. (23). One possible reason for this could be because the cylindrical shape used in the VSM model is closer to the shape of the particles in Fig. 1 than the ellipsoidal shape used in the LW model. This thinking is supported by the fact that the LW model gives a level of fit to a system of spherical particles which is

[6]The values of $\lambda = 0.01$ and $\lambda = 0.2$ were used in Eq. (23) for the VSM and LW model respectively [19]

comparable to the level of fit obtained with the VSM model for the needle particles in Fig. 1 [19]. This situation demonstrates the important role of the geometrical shape chosen to model a particular system of particles. The closer the geometrical shape chosen is to the actual shape of the particles, the better the fits obtained.

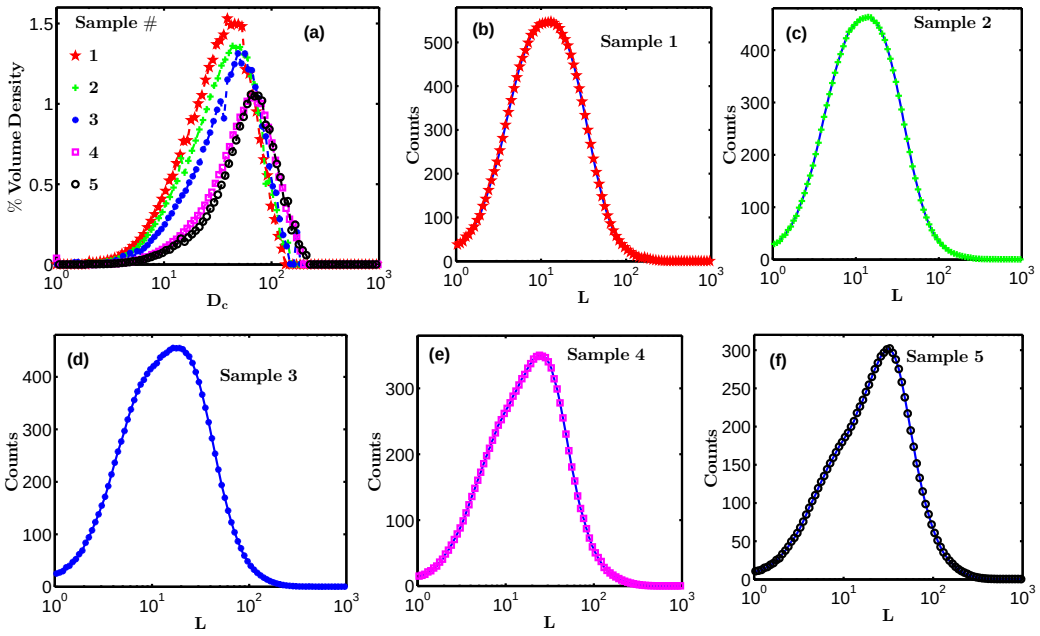

Figure 7: (a) The recovered volume based PSDs calculated from the objective function in Eq. (30) for $\lambda = 0$ [19] (with the VSM model) at the minimum aspect ratios (shown in Fig. 6(b)) for each Sample. (b)-(f) Calculated (symbols) and measured (solid line) Chord Length Distributions for the Samples indicated in each Figure. The calculated CLDs were obtained by solving the forward problem in Eq. (4) using the number based PSD which minimise the objective function in Eq. (23) for $\lambda = 0.01$ [19].

Figure 7(a) shows the volume based PSD calculated by minimising the objective function f_3 in Eq. (30) using the optimum aspect ratios in Fig. 6(b)[7]. This is the case of the VSM model. The transformation matrix $\tilde{\mathbf{A}}^o$ used in Eq. (30) was constructed using the optimum particle size range obtained by the inversion algorithm and aspect ratios shown in Fig. 6(b). The matrix $\tilde{\mathbf{A}}^o$ is then weighted as in Eq. (29)(a) to obtain the matrix

[7]The values of $\lambda = 0$ and $\lambda = 10^{-14}$ were used in Eq. (30) for the VSM and LW models respectively.

$\overline{\mathbf{A}}^o$. The CLD $\mathbf{C}^o$ was constructed from the matrix $\tilde{\mathbf{A}}^o$ using the number based PSD (using Eq. (25)) obtained at the optimum particle size range and aspect ratios shown in Fig. 6(b). The volume based PSD $\tilde{\mathbf{X}}^v$ normalised and rescaled as in Eq. (32) are shown in Fig. 7(a).

The PSDs in Fig. 7(a) are shown as a function of characteristic size D_c. This is comparable to the data from laser diffraction in Fig. 2(a) and EQPC diameter in Fig. 3(a). The particle sizes in Fig. 7(a) cover a range of $D_c \approx 7\mu$m and $D_c \approx 100\mu$m. The modes of the distributions cover a range of $D_c \approx 40\mu$m and $D_c \approx 70\mu$m with the sizes increasing from sample 1 to sample 5. This is consistent with the data from laser diffraction in Fig. 2(a) where the diameters cover a range of about 10μm to about 200μm. The modes of the distributions cover a range about 20μm to about 100μm with the particle sizes increasing from sample 1 to sample 5. Similarly, the EQPC diameters in Fig. 3(a) cover a range of about 20μm to about 200μm with the modes running from about 50μm to about 100μm, and the sizes increase from sample 1 to sample 5. This level of agreement of calculated with experimental data demonstrates the level of accuracy that can be achieved with this algorithm.

The symbols in Figs. 7(b) to 7(f) show the calculated (with the VSM model) CLDs for the five samples in Fig. 1. The CLDs were calculated from Eq. (4) using the number based PSD which minimises the objective function f_2 in Eq. (23). The calculations were done at the optimum aspect ratios in Fig. 6(b). The blue solid lines in Figs. 7(b) to 7(f) are the experimentally measured CLDs for the five samples shown in Fig. 2(b). The agreement between the calculated CLDs and the experimentally measured CLDs in Figs. 7(b) to 7(f) is near perfect.

Figure 8(a) shows the volume based PSDs for the five samples in Fig. 1 calculated with the LW model. The calculations were done in a similar manner as in Fig. 7(a). The distributions are plotted as a function of the characteristic size D_e which are comparable to the laser diffraction data in Fig. 2(a) and EQPC data in Fig. 3(a). The level of consistency of the volume based PSDs in Fig. 8(a) to the particle sizes in Figs. 2(a) and 3(a) is similar to the case of Fig. 7(a). The range of particle sizes in Fig. 8(a) and the modes of the distributions in Fig. 8(a) are close to the measured data in Figs. 2(a) and 3(a). However, the calculated PSDs in Fig. 8(a) contain spikes close to $D_e = 100\mu$m for sample 2 and sample 5. This may be due to the lower level of fit of the calculated data (using the LW model) with the needle data which may be partly due to the shape effect discussed earlier.

The symbols in Figs. 8(b) to 8(f) show the calculated (with the LW

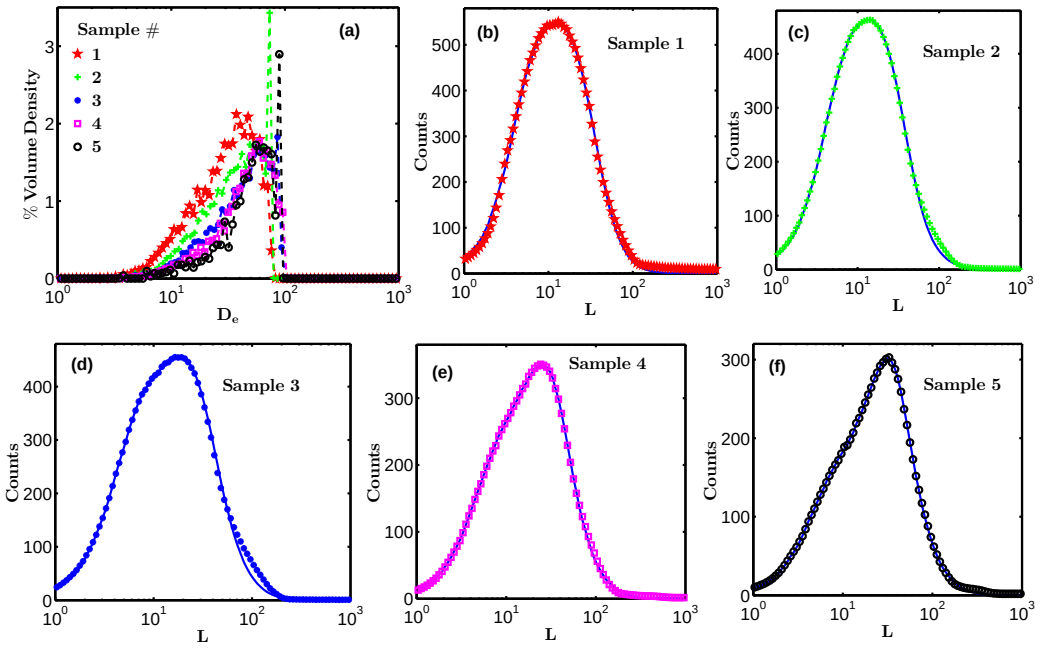

Figure 8: Similar to Fig. 7 obtained with the LW model. In this case the volume weighted PSDs were obtained at $\lambda = 10^{-14}$ from Eq.(30), while the CLDs correspond to number distributed PSD obtained at $\lambda = 0.2$ from Eq. (23) [19].

model) CLDs for the samples in Fig. 1. The calculations were done in a manner similar to the case of Figs. 7(b) to 7(f). However, the calculated CLDs in Figs. 8(b) to 8(f) show slight mismatch with the experimental data unlike the case of Figs. 7(b) to 7(f) where the match is near perfect.

Apart from the shape effect, another possible reason for the different levels of agreement between calculated data with the two models and experimental data could be because different kinds of approximations were made in the formulation of the models. The VSM model considers all possible 3 D orientations of the cylinder in the computation of the cylindrical PDF [11]. However, the LW model considers only one 2 D projection of the ellipsoid where the major and minor axes are parallel to the $x - y$ plane [9]. Furthermore the VSM model makes small angle approximations in other to obtain an analytical expression for the cylindrical PDF [11]. These different approximations possibly contribute to the different levels of agreement of the predictions of the two models with experimental data.

Figure 9(a) shows the volume based PSD calculated with the VSM model

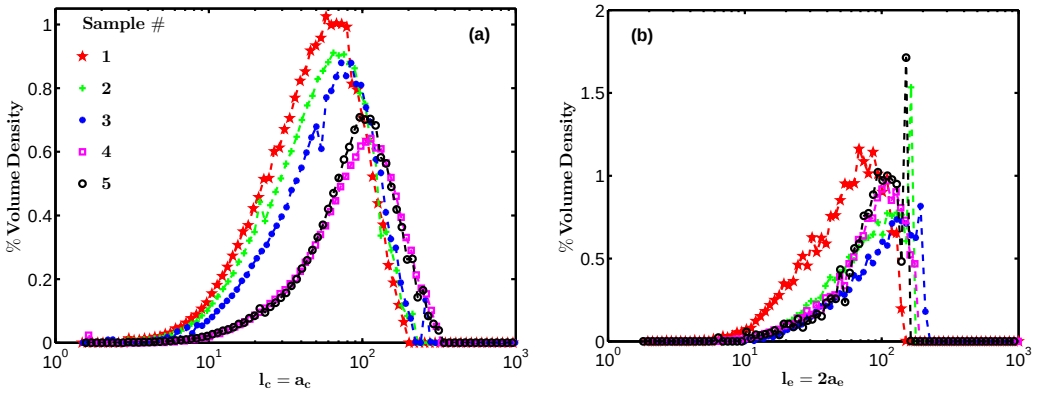

Figure 9: Particle lengths for the five samples calculated with (a) the VSM model and (b) the LW model.

plotted as a function of the characteristic length $l_c = a_c$ (the height of the cylinder). This data is comparable to the Feret Max data in Fig. 3(b). The Feret Max data covers a range of about 100μm to about 800μm for sample 5, although sample 1 is significantly shifted to the left with a range of about 20μm to about 500μm. The characteristic lengths predicted by the VSM model in Fig. 9(a) are short of the Feret Max data in Fig. 3(b) because the aspect ratios predicted by the VSM model in Fig. 6(b) are higher than the estimated aspect ratios in Fig. 3(d). This implies that the VSM model predicts needles that are slightly thicker and shorter than the actual needles in the samples.

A similar situation holds for the LW model where the predicted ellipsoids heights (l_e in Fig. 9(b)) are short of the Feret Max measurements in Fig. 3(b). Similarly, the aspect ratios predicted by the LW model in Fig. 6(d) are higher than the estimated aspect ratios in Fig. 3(d). This again shows that the LW model predicts needles which are slightly thicker and shorter than the actual needles in the samples.

Even though the predicted lengths (l_c and l_e) do not have a perfect match with the measured Feret Max data, the trend in the lengths of needles from sample 1 to sample 5 in Fig. 3(b) are consistent with the trend in needle lengths from sample 1 to sample 5 in Fig. 9(a). However, the trend in needle lengths in Fig. 9(b) are not so consistent with the trend in needle lengths in Fig. 3(b) moving from sample 1 to sample 5. This is because the LW model predicts smaller aspect ratios for sample 2 and sample 3 in Fig. 6(d) resulting in a right shift of the distributions for sample 2 and sample 3 in

Fig. 9(b).

7. Conclusion

The technique described here is model independent as can be seen by the level of agreement of the calculated PSDs (by two different models) with experimentally measured PSDs. The shape information recovered by this technique also shows close agreement with estimates from experimental data. However, there is still room for improvement. The calculated particle sizes deviate from the experimentally measured sizes by about a factor of two. This is most pronounced in the case of the calculated needle lengths in Fig. 9 and the Feret Max measurements in Fig. 3(b). The situation also shows up in the needle thickness. The algorithm predicts thicker needles in Fig. 6 when compared with estimated needle thickness in Fig. 3(d). This demonstrates the well known fact that very accurate size and shape information cannot be retrieved from FBRM data alone. Hence the technique described here will greatly benefit from additional information say from a suitable imaging technique. This is the line of action that will be pursued in future development.

It should be noted that the samples from which the data used for validation here were prepared under well controlled conditions. Furthermore, the materials have been treated as though all the needles in a particular sample have the same aspect ratio. The technique may not be very successful if the needles in a particular sample have a wide range of aspect ratios. The extension of the technique to account for this situation has been reserved for future work.

The LW and VSM models employed in this work will break down in the case where the materials are highly transparent. In this situation most of the light from the FBRM probe will be transmitted by the particles which then results in chord splitting [12]. The chord lengths reported in this case may not be an accurate representation of particle sizes. The LW and VSM models do not account for this effect. A suitable way to incorporate optical properties of materials into this technique will be made in future developments.

Acknowledgement

The authors wish to thank the EPSRC (grant number EP/K014250/1) for generous funding for this project.

References

[1] C. Washington, Particle size analysis in pharmaceutics and other industries, Ellis Horwood Limited, Chichester, England, 1992.

[2] J. Heinrich, J. Ulrich, Application of laser-backscattering instruments for in situ monitoring of crystallization process - a review, Chem. Eng. Technol. 35 (6) (2012) 967–979.

[3] A. Tadayyon, S. Rohani, Determination of particle size distribution by Par-Tec©100: modeling and experimental results, Part. Part. Syst. Charact. 15 (1998) 127–135.

[4] A. Ruf, J. Worlitschek, M. Mazzotti, Modeling and experimental analysis of PSD measurements through FBRM, Part. Part. Syst. Charact. 17 (2000) 167–179.

[5] A. R. Heath, P. D. Fawell, P. A. Bahri, J. D. Swift, Estimating average particle size by focused beam reflectance measurement (FBRM), Part. Part. Syst. Charact. 19 (2002) 84–95.

[6] E. J. W. Wynn, Relationship between particle-size and chord-length distributions in focused beam reflectance measurement: stability of direct inversion and weighting, Powder Technology 133 (2003) 125–133.

[7] J. Worlitschek, M. Mazzotti, Choice of the focal point position using Lasentec FBRM, Part. Part. Syst. Charct. 20 (2003) 12–17.

[8] J. Worlitschek, T. Hocker, M. Mazzotti, Restoration of PSD from chord length distribution data using the method of projections unto convex sets, Part. Part. Syst. Charct. 22 (2005) 81–98.

[9] M. Li, D. Wilkinson, Determination of non-spherical particle size distribution from chord length measurements. part 1: theoretical analysis., Chemical Engineering Science 60 (2005) 3251–3265.

[10] M. Li, D. Wilkinson, K. Patchigolla, Determination of non-spherical particle size distribution from chord length measurements. part 2: experimental validation, Chemical Engineering Science 60 (2005) 4992–5003.

[11] A. Vaccaro, J. Sefcik, M. Morbidelli, Modeling focused beam reflectance measurement and its application to sizing of particles of variable shape, Part. Part. Syst. Charact. 23 (2006) 360–373.

[12] N. Kail, H. Briesen, W. Marquardt, Advanced geometrical modeling of focused beam reflectance measurements (FBRM), Part. Part. Syst. Charact. 24 (2007) 184–192.

[13] N. Kail, H. Briesen, W. Marquardt, Analysis of FBRM measurements by means of a 3D optical model, Powder Technology 185 (2008) 211–222.

[14] N. Kail, W. Marquardt, H. Briesen, Estimation of particle size distributions from focused beam reflectance measurements based on an optical model, Chemical Engineering Science 64 (2009) 984–1000.

[15] S. Scheler, Ray tracing as a supportive tool for interpretation of FBRM signals from spherical particles, Chemical Engineering Research and Design 101 (2013) 503–514.

[16] E. F. Hobbel, R. Davies, F. W. Rennie, T. Allen, L. E. Butler, E. R. Waters, J. T. Smith, R. W. Sylvester, Modern methods of on-line size analysis for particulate streams, Part. Part. Syst. Charact. 8 (1991) 29–34.

[17] M. J. H. Simmons, P. A. Langston, A. S. Burbidge, Particle and droplet size analysis from chord distributions, Powder Technology 102 (1999) 75–83.

[18] P. A. Langston, A. S. Burbidge, T. F. jones, M. J. H. Simmons, Particle and droplet size analysis from chord measurements using Bayes' theorem, Powder Technology 116 (2001) 33–42.

[19] See the supplementary information for further comparison of calculations with experimentally measured quantities. The supplementary information also contains calculations not shown here.

[20] P. Hamilton, D. Littlejohn, A. Nordon, J. Sefcik, P. Slavin, Validity of particle size analysis techniques for measurement of the attrition that occurs during vacuum agitated powder drying of needle-shaped particles, Analyst 137 (2012) 118–125.

[21] P. Hamilton, D. Littlejohn, A. Nordon, J. Sefcik, P. Slavin, P. Dallin, J. Andrews, Studies of particle drying using non-invasive Raman spectroscopy and particle size analysis, Analyst 136 (2011) 2168–2174.

[22] S. Boyd, L. Vandenberghe, Convex Optimization, Cambridge University Press, Cambridge University Press, Cambridge, UK, 2004.

[23] M. Kaasaleinen, J. Torppa, Optimization methods for asteroid lightcurve inversion i. shape determination, Icarus 153 (2001) 24–36.

[24] R. G. Holdich, Fundamentals of Particle Technology, Midland Information Technology and Publishing, Leicestershire, UK, 2002.